# PCCP

## Accepted Manuscript

# Mechanical properties of monolayer penta-graphene and phagraphene: a first-principles study

*Hao Sun[a*], Sankha Mukherjee[b*], Chandra Veer Singh[a, b]*

[a]Department of Mechanical and Industrial Engineering, University of Toronto, Toronto, ON, M5S 3G8, Canada

[b]Department of Materials Science and Engineering, University of Toronto, Toronto, ON, M5S 3E4, Canada

Two new graphene allotropes, penta-graphene and phagraphene, have been proposed recently with unique electronic properties, e.g. quasi-direct band gap, direction-dependent Dirac cones and tunable Fermi velocities. However, their mechanical properties have not been fully studied yet. In this work, we have performed extensive density functional theory calculations to evaluate the mechanical properties of these two materials and compared with graphene, graphane, and pentapthite. Our simulations show that the ultimate tensile strength (UTS) and the strain corresponding to UTS in both penta-graphene and phagraphene are smaller than that of graphene. A complete set of nonlinear anisotropic elastic constants up to the fourth order have been determined for these two allotropes using the tenets of continuum mechanics by fitting the stress-strain responses under uniaxial and biaxial tension until the point of fracture. We propose a new physical explanation for penta-graphene's negative Poisson's ratio based on the atomic de-wrinkling mechanism, driven by the local Hellman–Feynman force on each atom. Additionally, we used charge density plot and virtual Scanning Tunneling Microscopy images to analyze the initiation of fracture under uniaxial and biaxial tensile loading in these two materials. The charge density plots reveal that the charge density in $sp^3$ bonds is lower than the $sp^2$ bonds. In phagraphene, all the broken bonds were found to belong to the largest carbon ring in the structure.

* Both authors contributed equally to this work.

# 1. INTRODUCTION

Recently, two new graphene allotropes, penta-graphene[1] and phagraphene[2] have been proposed with remarkable material properties that can outperform graphene. For example, unlike graphene, the nanotubes made of penta-graphene are semiconducting regardless of their chirality[1], thereby, offer benefits over conventional carbon nanotubes which can be either metallic or semiconducting[3]. Additionally, penta-graphene's quasi-direct band gap[1] can be useful for optoelectronic and photovoltaic applications[3]. The structure of phagraphene is composed of rings containing five, six, and seven atoms, which is topologically similar to hybrid boron nitride[4]. Recent research suggests that phagraphene possesses direction-dependent Dirac cones with tunable Fermi velocities which are robust against externally applied strain[2]. Interestingly, hybrid boron nitride also possess unique electronic and magnetic properties, such as, semiconductivity with notably reduced band gap compared to the normal boron nitride nanoribbons[4]. Furthermore, with the knowledge of mechanical properties of phagraphene and penta-graphene, we can tailor their electronic properties by strain engineering[5]. Nonetheless, since these materials are ultrathin due to their two-dimensional (2D) nature, they are susceptible to external influences, including mechanical deformation[5]. Therefore, an in-depth understanding of their structure-property relationship is necessary for practical application.

Efforts have been made to understand the structural stability[6] and the effects of doping[7] and functionalization[8] on the mechanical properties of penta-graphene. Zhang[1] et al. performed density functional theory (DFT) calculations and reported that, (a) penta-graphene is strong with an ultimate tensile strength (UTS) of 20 N/m under biaxial tensile loading, and (b) it possesses a negative Poisson's ratio ($\nu$). The negative Poisson's ratio of penta-graphene was attributed to the Coulombic repulsion between the nearby $sp^3$ bonds – a mechanism observed in isolated $CH_4$ molecules[1]. In recent years, research has been undertaken to understand the effect of doping[7] and functionalization[8] on the mechanical properties of penta-graphene. Using DFT calculations, Zhang[7] et. al. created penta-$CN_2$ by replacing the $sp^3$ hybridized carbon atoms in penta-graphene with nitrogen atoms, which resulted in a significantly increased axial Young's modulus ($E$) of 319 N/m, much higher than that of pristine penta-graphene (~263.8 N/m[8]). This improvement in axial stiffness was attributed to the stronger interatomic bonding between the carbon and nitrogen atoms than the covalent carbon-carbon bonds in pristine penta-graphene[9]. Li et al.[8] reported that the electronic and mechanical properties of penta-graphene can be tuned by functionalizing it with hydrogen and fluorine, e.g. converting the material from semiconducting to insulating and turning its negative Poisson's ratio into positive. The structure of phagraphene can be considered as a defective form of graphene. Graphene with defect has a much lower UTS than that of pristine graphene[10–13]. Other graphene allotropes, like OcGr, PeHe-A, and PeHe-B, are also kind of defective graphene, and they are weaker than graphene[14]. Therefore, since phagraphene also can be considered as defective graphene, it is reasonable to predict that it is weaker than graphene. However, since, it has just been discovered last year, very few article has made an attempt to evaluate its mechanical properties.

The nonlinear elastic constants of graphene and its allotropes' can be evaluated by fitting their nonlinear elastic stress-strain curves to higher order fitting polynomials of strain[15–

[17,24]. These fitting constants are useful in studies related to the thermal expansion, phonon–phonon interaction, and finite element analysis of these materials. However, despite the importance, a study of the nonlinear elastic constants of phagraphene and penta-graphene, is still missing. In this paper, we performed extensive theoretical analysis to understand the structure and mechanical relations of penta-graphene and phagraphene. Using first-principle DFT computations, stress-strain responses under uniaxial and biaxial loading were simulated, and the complete set of anisotropic nonlinear elastic constants were estimated by fitting the stress-strain data to the fourth order continuum elasticity theory. Additionally, we proposed a new explanation based on an atomic de-wrinkling mechanism for understanding the origin of negative Poisson's ratio in penta-graphene. The paper ends by analyzing the fracture behavior in penta-graphene and phagraphene using charge density analysis and virtual Scanning Tunneling Microscopy (STM) images.

## 2. METHODOLOGY

Plane wave based DFT calculations were performed using the Quantum Espresso software package[18] and Perdew–Burke–Ernzerh (PBE) exchange–correlation functional[19] within the generalized gradient approximation (GGA). Kinetic energy cut-offs of 60 Ry and 480 Ry were used for the calculation of wavefunction and charge density, respectively. The convergence criterion for the self-consistent field (SCF) procedure was set to $1.0 \times 10^{-6}$ Ry. Brillouin-zone integrations were performed using a Monkhorst−Pack grid[20] of $13 \times 13 \times 3$ k-points. A 20 Å vacuum layer was added to the simulation box to avoid interaction between adjacent images. Each system was initially relaxed with variable cell sizes using conjugate gradient minimization technique until the magnitude of the residual Hellman–Feynman force on each atom was less than 0.001 Ry per Bohr. After the initial relaxation, the unit cells (marked by pink in Figure 1) were subjected to different magnitudes of uniaxial, equal-biaxial strains in the $x$ and $y$ directions (i.e. 1 and 2 directions, respectively). The structures were deformed by incrementally dilating the unit cells along the loading direction and applying an equal affine transformation to the atomic positions, followed by an energy minimization routine. During this relaxation step, the cell dimensions were fixed to preserve the overall strain loading on the deformed configuration. The atomic positions, charge density, and virtual STM were visualized using the XCrySDen[21] package.

True (Cauchy) stress was calculated for each optimized structure from the pressure tensor. Cauchy stress was converted to the 2nd Piola-Kirchoff (P-K) stress $\Sigma$ (N/m) through the deformation tensor ($F$) using the relation[22]

$$\Sigma = JF^{-1}\sigma(F^{-1})^{T}, \qquad J = det(F). \tag{1}$$

We assumed a thickness of 3.45 Å for phagraphene, same as graphene[23]. For penta-graphene, the thickness was assumed to be 4.65 Å (given the monolayer thickness is 3.45 Å and 1.2 Å is the interplanar distance).

The nonlinear elastic constants were evaluated by performing a least-squares fitting to the 2nd P-K stress-strain data following the continuum description of nonlinear elasticity of graphene proposed by Wei et al[15]. The mechanical response of graphene allotropes under uniaxial Lagrangian strain ($\eta$) along the $x$ direction (i.e., 1 direction) can be represented using the Voigt notation, which is given by

$$\Sigma_1^1 = C_{11}\eta_1 + \frac{1}{2}C_{111}\eta_1^2 + \frac{1}{6}C_{1111}\eta_1^3 + \frac{1}{24}C_{11111}\eta_1^4 \tag{2}$$

$$\Sigma_2^1 = C_{12}\eta_1 + \frac{1}{2}C_{112}\eta_1^2 + \frac{1}{6}C_{1112}\eta_1^3 + \frac{1}{24}C_{11112}\eta_1^4 \tag{3}$$

$$\Sigma_6^1 = 0 \tag{4}$$

In the case of uniaxial loading along the $y$ axis, where $\eta_1 = 0, \eta_2 \geq 0, \eta_6 = 0$, the mechanical response is given by

$$\Sigma_1^2 = C_{12}\eta_2 + \frac{1}{2}(C_{111} - C_{222} + C_{112})\eta_2^2 + \frac{1}{12}(C_{1111} + 2C_{1112} - C_{2222})\eta_2^3 + \frac{1}{24}C_{12222}\eta_2^4 \tag{5}$$

$$\Sigma_2^2 = C_{22}\eta_2 + \frac{1}{2}C_{222}\eta_2^2 + \frac{1}{6}C_{2222}\eta_2^3 + \frac{1}{24}C_{22222}\eta_2^4 \tag{6}$$

$$\Sigma_6^2 = 0 \tag{7}$$

Under equal-biaxial loading, the constitutive equations are given by

$$\Sigma_1^{biax} = (C_{11} + C_{12})\eta + \frac{1}{2}(2C_{111} - C_{222} + 3C_{112})\eta^2$$
$$+ \frac{1}{6}\left(\frac{3}{2}C_{1111} + 4C_{1112} - \frac{1}{2}C_{2222} + 3C_{1122}\right)\eta^3$$
$$+ \frac{1}{24}(3C_{11111} + 10C_{11112} - 5C_{12222} + 10C_{11122} - 2C_{22222})\eta^4 \tag{8}$$

$$\Sigma_1^{biax} = \Sigma_2^{biax} \tag{9}$$

$$\Sigma_6^{biax} = 0 \tag{10}$$

Eqs. (2-10) are valid for finite strains under arbitrary in-plane tensile loading when the bending stiffness is negligible. It is, however, important to note that in paper by Wei's et al.[15], Eq. (6) assumed $C_{11} = C_{22}$, which is not accurate for systems with significant anisotropic mechanical behavior. Therefore, in order to accommodate the anisotropic effects, we evaluated $C_{22}$ separately.

## 3. RESULTS AND DISCUSSION

### 3.1 Tensile Stress-strain Relationship

Cranford[6] found that the pentagonal ring in penta-graphene, which is composed of sp$^3$ hybridized bonds, undergoes an irreversible transformation under the influence of mechanical strain or temperature and converts into a purely hexagonal ring composed of sp$^2$ hybridized bonds. In our study, we considered the mechanical deformation of penta-graphene and phagraphene at ground energy state. The second P–K stress versus Lagrangian strain responses of penta-graphene and phagraphene for in-plane uniaxial and biaxial tensile loading are shown in Figure 2 (a), and (b). Since penta-graphene is symmetric to 90° rotations, its mechanical behavior in the in-plane directions is identical. For strains smaller than 0.1, both the materials were found to follow a linear stress-strain response. For strains larger than 0.1, the 2nd Piola-Kirchoff (P-K) stresses behaved

nonlinearly with increasing strains. Both $\Sigma_1^1$ and $\Sigma_2^2$ in penta-graphene are negative due to its negative Poisson's ratio. Figure 2 (c) and (d) represent the strain energy increase in penta-graphene and phagraphene as a function of Lagrangian strain for multiaxial tensile deformation. In both the materials, for strains smaller than 0.1, the strain energy obeys a quadratic relation with $\eta$. This result suggests that a linear relationship exists between stress and strain for small deformations ($\eta < 0.1$). However, for $\eta > 0.1$, nonlinear elastic behavior becomes dominant in both the materials.

The nonlinear stress-strain responses presented in Figure 2 (a), (b) are qualitatively similar to theoretical calculations reported for graphene[15] and its allotropes[15–17,24]. As described earlier, we fit simulated stress-strain data to Eqs. (2-10) to find out the nonlinear elastic constants. Subsequently, these constants are used to calculate the $E$ and $\nu$ using the following

$$E = \frac{C_{11}^2 - C_{12}^2}{C_{11}}, \quad \nu = \frac{C_{12}}{C_{11}}. \tag{11}$$

The magnitudes of UTS, the strain corresponding to UTS point ($\eta_u$), $E$, and $\nu$ for penta-graphene, phagraphene, graphene[15], graphane[24], and pentaheptite[17] are listed in Table I. Graphene possesses ultrahigh $E$ and UTS compared to the rest of the materials. Interestingly, for $x$-uniaxial tension, graphane and pentaheptite have a higher $\eta_u$ than graphene.

The differences in the mechanical properties of different graphene allotropes can be attributed to the differences in their area densities and the nature of the C-C bonds[25,26] (see Table I). Both pentaheptite[17] and phagraphene possess area densities smaller than graphene, leading to fewer bond connections and consequently a smaller UTS and $E$. Although, penta-graphene has a higher area density than graphene due to its three-layered structure, 80% of its carbon bonds are sp$^3$ hybridized, whereas the carbon-carbon bonds in graphene are sp$^2$ hybridized. Graphane has a honey-comb like structure similar to graphene, but, all the carbon atoms are sp$^3$ hybridized due to the C-H bond. The UTS and $E$ in graphene, penta-graphene, and graphane decrease as the percentage of sp$^3$ bonds increase (graphene > penta-graphene > graphane). Recently, using *ab initio* molecular dynamics simulations, Wang et al.[8] attached hydrogen atoms to the carbon atoms in penta-graphene with sp$^2$ bonds, which resulted in a structure with 100% percent sp$^3$ hybridized bonds. As a result, the Young's modulus of the structure reduced from 263.8 *N/m* to 205.5 *N/m* for hydrogenated penta-graphene. These findings are in line with our observation that sp$^3$ hybridization deteriorates the mechanical properties of graphene allotropes.

Penta-graphene possesses a negative Poisson's ratio (-0.078) which is much lower than that of graphene (0.169[14]). This behavior has been attributed to the bond rotation of the sp$^3$ bonds by Zhang[1] et al. However, in penta-graphene bond rotations are restricted due to the geometrical constraints imposed by neighboring carbon atoms. Our simulations did not show any significant bond rotation up to a strain of 0.2 under both uniaxial and biaxial loading (Figure 5). Recently, single-layer black phosphorus which has a puckered structure has been reported to possess a negative Poisson's ratio under uniaxial deformation in the out-of-plane direction[27]. Wrinkled graphene papers also have negative

Poisson's ratio[28]. During tensile stretching, the de-wrinkling and unfolding processes give rise to a negative Poisson ratio in the graphene papers. Similarly, in penta-graphene, the carbon atoms are not coplanar, this nano-wrinkled structure introduces similar local flexion which resists deformation in the transverse direction. In our simulations, de-wrinkling mechanism was observed in penta-graphene during tensile deformation. Figure 3 (a) and (b) represent the atomic configurations and residual Hellman–Feynman force on each atom in penta-graphene for a uniaxial tensile strain of 7%. The length and the direction of the green arrows represent the relative magnitudes and the directions of the Hellman–Feynman forces, respectively. These forces determine the direction of movement of each atom during deformation. It can be seen from Figure 3(c) that during deformation, due to the Hellman–Feynman force, the atoms in the P1 and P3 planes move towards each other in the $z$ direction and move away from each other in the $y$-direction, causing expansion of the unit cell in the direction perpendicular to the applied deformation and contraction in the out-of-plane direction.

### 3.2 Nonlinear Elastic Constants

The fifteen fourth-order elastic constants of penta-graphene and phagraphene were calculated by fitting the simulated stress-strain responses to Eqs. (2-10). The magnitudes of the elastic constants of these two structures are listed in Table II. Additionally, for comparison, we presented the values of the nonlinear elastic constants of graphene[15] in Table II. It can be seen that the $C_{111}$ and $C_{222}$ are negative for all the allotropes. As a result, the structures show mechanical strain softening for increased values of strain. Our calculations also predict that among all the allotropes, Graphene possess the largest $C_{11}$ ($358.1 N/m$[15]), while penta-graphene has the lowest $C_{11}$ ($275.71$ $N/m$). This observation is in sync with the fact that penta-graphene has the lowest UTS and Young's modulus while graphene has the largest UTS, and $E$. We calculated the pressure-dependent second-order elastic constants ($\tilde{C}_{11}$, $\tilde{C}_{12}$) of pentagraphene and phagraphene using the following expressions[29]

$$\tilde{C}_{11} = C_{11} - (C_{111} + C_{112})\frac{1-v}{E}P, \tag{12}$$

$$\tilde{C}_{12} = C_{12} - C_{112}\frac{1-v}{E}P, \tag{13}$$

where $P$ is the in-plane pressure. It can be seen from Figure 4 (a), in both the structures, the second-order elastic moduli increased linearly with pressure. The rate of increase of elastic moduli is highest in graphene compared to penta-graphene and phagraphene. We found that the Poisson's ratio in graphene and phagraphene decreases with pressure, unlike in penta-graphene wherein Poisson's ratio increases with pressure (Figure 4 (b)). The Poisson's ratio of phagraphene (0.41~0.28) is larger than that of graphene (0.28~1.6) and penta-graphene (-1.7~-0.078) for the entire pressure range studied here. Since a perfectly incompressible material has a Poisson's ratio of 0.5, phagraphene is observed to conserve volume better than graphene and penta-graphene. Generally, for most two-dimensional structures, the absolute value of Poisson's ratio decreases with an increasing in-plane pressure, which suggests that 2D materials are easily compressed than sheared for increased in-plane pressures.

### 3.3 Fracture Mechanics

According to previous research, in graphene, atomic bonds that make a small angle or are parallel to the direction of loading are susceptible to failure[16]. In penta-graphene, the $sp^3$ hybridized bonds break first under both uniaxial (Figure 5(a)) and biaxial (Figure 5(c)) tensile loading. A complete fracture of the entire structure occurs after the rupture of the first bond. To understand the fracture behavior in depth, we utilized charge density and virtual STM images; virtual STM images can probe unoccupied regions for electrons[30]. Since, in penta-graphene atoms are not coplanar, the virtual STM images showed contrasting behavior for the broken and unbroken bonds. As shown in Figure 5 (b), for atoms in the P1 plane in penta-graphene under uniaxial loading, the relative electron density in the broken $sp^3$ bonds are smaller than the unbroken bonds. On the other hand, under biaxial tension, the unbroken $sp^2$ bonds have falcate shapes. Isolated atoms with failed $sp^3$ bonds appear as a circle in the STM images. Since, for any given quantum number, electrons in the s orbitals are nearer to the nucleus than the electrons in the p orbitals. Generally, the more s character the bond has, the shorter the bond length is and the more tightly held the bond will be. Geometrically, the $sp^3$ bonds in penta-graphene (1.55 Å) are longer than the $sp^2$ bonds (1.34 Å), and the magnitude of charge density at the center of a $sp^3$ bond is smaller than that of a $sp^2$ bond. In Figures 5 (f) we show the charge densities in the P1 and P4 planes of penta-graphene. The maximum value of the charge density at the center of the $sp^2$ bonds in the P1 plane is $0.3695Å^{-2}$, which is much higher than that of the $sp^3$ bonds in the P4 plane ($0.2768Å^{-2}$). A higher charge density indicates a stronger interaction in $sp^2$ bonds compared to $sp^3$ bonds, resulting in higher bond strength. As a result, the magnitude of the stress needed for fracture initiation is smaller for graphane (composed of $sp^3$ hybridized bonds only) compared to penta-graphene.

In phagraphene, for uniaxial loading in the $x$ direction (see Figure 6(a) and (b)), three bonds fail simultaneously. During $y$-uniaxial tension (see Figure 6(c) and (d)), two bonds brake, as a result, three carbon rings combine into a single ring. Under biaxial tension (see Figure 6(e) and (f)), the broken bonds cut all the units and the whole structure fails, completely. In all the cases, all the broken bonds belong to the original largest carbon ring. Therefore, the largest ring is the weakest unit in phagraphene.

### 4. CONCLUSION

We characterized the mechanical behavior of monolayer penta-graphene and phagraphene under multi-axial loading using DFT calculations. Simulated results predict that both of the structures have lower UTS and $E$ compared to graphene. A fourth order continuum elasticity theory was used to evaluate fifteen nonlinear elastic constants of the materials based on the simulated stress-strain data. The negative Poisson's ratio in penta-graphene was found to originate from the de-wrinkling of different atomic planes during tensile deformation. Charge density and virtual STM images were utilized to determine the fracture pathways in both the materials. Both the structure either underwent a structural transition generating larger carbon rings or failed completely after the breakage of the first bond. In penta-graphene, the $sp^3$ bond is more vulnerable to failure than the

$sp^2$ bond due to longer bond length and lower charge density. In phagraphene, the weakest unit is the largest carbon ring, which is the origin of fracture under multi-axial loading.

## ACKNOWLEDGEMENTS

## REFERENCE

1   S. Zhang, J. Zhou, Q. Wang, X. Chen, Y. Kawazoe and P. Jena, *Proc. Natl. Acad. Sci.*, 2015, **112**, 2372–2377.

2   Z. Wang, X.-F. Zhou, X. Zhang, Q. Zhu, H. Dong, M. Zhao and A. R. Oganov, *Nano Lett.*, 2015, **15**, 6182–6186.

3   Z. G. Yu and Y.-W. Zhang, *J. Appl. Phys.*, 2015, **118**, 165706.

4   S. Tang and S. Zhang, *J. Phys. Chem. C*, 2013, **117**, 17309–17318.

5   F. Guinea, M. I. Katsnelson and A. K. Geim, *Nat. Phys.*, 2010, **6**, 30–33.

6   S. W. Cranford, *Carbon*, 2016, **96**, 421–428.

7   S. Zhang, J. Zhou, Q. Wang and P. Jena, *J. Phys. Chem. C*, 2016, **120**, 3993–3998.

8   X. Li, S. Zhang, F. Q. Wang, Y. Guo, J. Liu and Q. Wang, *Phys Chem Chem Phys*, 2016, **18**, 14191–14197.

9   V. Levitin, *Interatomic Bonding in Solids: Fundamentals, Simulation, and Applications*, Wiley-VCH Verlag GmbH & Co. KGaA, Weinheim, Germany, 2013.

10  Y. Wei, J. Wu, H. Yin, X. Shi, R. Yang and M. Dresselhaus, *Nat. Mater.*, 2012, **11**, 759–763.

11  K. Kim, V. I. Artyukhov, W. Regan, Y. Liu, M. F. Crommie, B. I. Yakobson and A. Zettl, *Nano Lett.*, 2012, **12**, 293–297.

12  Z. Song, V. I. Artyukhov, J. Wu, B. I. Yakobson and Z. Xu, *ACS Nano*, 2015, **9**, 401–408.

13  T. Zhang, X. Li, S. Kadkhodaei and H. Gao, *Nano Lett.*, 2012, **12**, 4605–4610.

14  Z. G. Fthenakis and N. N. Lathiotakis, *Phys Chem Chem Phys*, 2015, **17**, 16418–16427.

15  X. Wei, B. Fragneaud, C. A. Marianetti and J. W. Kysar, *Phys. Rev. B*, 2009, **80**.

16  Q. Peng, W. Ji and S. De, *Phys. Chem. Chem. Phys.*, 2012, **14**, 13385.

17  Z. G. Fthenakis and N. N. Lathiotakis, *Phys Chem Chem Phys*, 2015, **17**, 16418–16427.

18  P. Giannozzi, S. Baroni, N. Bonini, M. Calandra, R. Car, C. Cavazzoni, D. Ceresoli, G. L. Chiarotti, M. Cococcioni, I. Dabo, A. Dal Corso, S. de Gironcoli, S. Fabris, G. Fratesi, R. Gebauer, U. Gerstmann, C. Gougoussis, A. Kokalj, M. Lazzeri, L. Martin-Samos, N. Marzari, F. Mauri, R. Mazzarello, S. Paolini, A. Pasquarello, L. Paulatto, C. Sbraccia, S. Scandolo, G. Sclauzero, A. P. Seitsonen, A. Smogunov, P. Umari and R. M. Wentzcovitch, *J. Phys. Condens. Matter*, 2009, **21**, 395502.

19  J. P. Perdew, K. Burke and M. Ernzerhof, *Phys. Rev. Lett.*, 1996, **77**, 3865–3868.

20  H. J. Monkhorst and J. D. Pack, *Phys. Rev. B*, 1976, **13**, 5188–5192.

21  A. Kokalj, *Comput. Mater. Sci.*, 2003, **28**, 155–168.

22  J. Bonet and R. D. Wood, *Nonlinear continuum mechanics for finite element analysis*, Cambridge University Press, Cambridge, UK ; New York, 2nd ed., 2008.

23  C. Galiotis, O. Frank, E. N. Koukaras and D. Sfyris, *Annu. Rev. Chem. Biomol. Eng.*, 2015, **6**, 121–140.

24  Q. Peng, Z. Chen and S. De, *Mech. Adv. Mater. Struct.*, 2015, **22**, 717–721.

25  Y. Y. Zhang, Q. X. Pei and C. M. Wang, *Appl. Phys. Lett.*, 2012, **101**, 081909.

26  S. W. Cranford, D. B. Brommer and M. J. Buehler, *Nanoscale*, 2012, **4**, 7797.

27  J.-W. Jiang and H. S. Park, *Nat. Commun.*, 2014, **5**.

28  J. N. Grima, S. Winczewski, L. Mizzi, M. C. Grech, R. Cauchi, R. Gatt, D. Attard, K. W. Wojciechowski and J. Rybicki, *Adv. Mater.*, 2015, **27**, 1455–1459.

29  S. Y. Davydov, *Phys. Solid State*, 2011, **53**, 665–668.

30  Z. Hou, X. Wang, T. Ikeda, K. Terakura, M. Oshima and M. Kakimoto, *Phys. Rev. B*, 2013, **87**.

Table I: UTS and corresponding $\eta_u$ for penta-graphene and phagraphene, compared with graphene

| | Graphene[15] | Penta-graphene | Phagraphene | Graphane[24] | Pentaheptite[17] |
|---|---|---|---|---|---|
| $x$-axial UTS (*N/m*) | 30.36 | 23.51 | 25.39 | 21.8 | 25.72 |
| $y$-axial UTS (*N/m*) | 28.56 | 23.51 | 25.57 | 19.1 | 24.08 |
| biaxial UTS (*N/m*) | 32.01 | 25.40 | 24.8 | 21.2 | - |
| $x$-axial $\eta_u$ | 0.22 | 0.18 | 0.18 | 0.25 | 0.24 |
| $y$-axial $\eta_u$ | 0.18 | 0.18 | 0.16 | 0.17 | 0.19 |
| Biaxial $\eta_u$ | 0.22 | 0.22 | 0.16 | 0.25 | - |
| Area density ($Å^{-2}$) | 0.379 | 0.453 | 0.368 | - | 0.367 |
| Poisson ratio $\nu$ | 0.169 | -0.078 | 0.255 | 0.076 | 0.253 |
| $E$ (N/m) | 348 | 277.99 | 292.92 | 249.3 | 292.26 |

Table II. Nonlinear independent elastic constants (N/m) of penta-graphene and phagraphene from DFT calculations, compared with graphene.

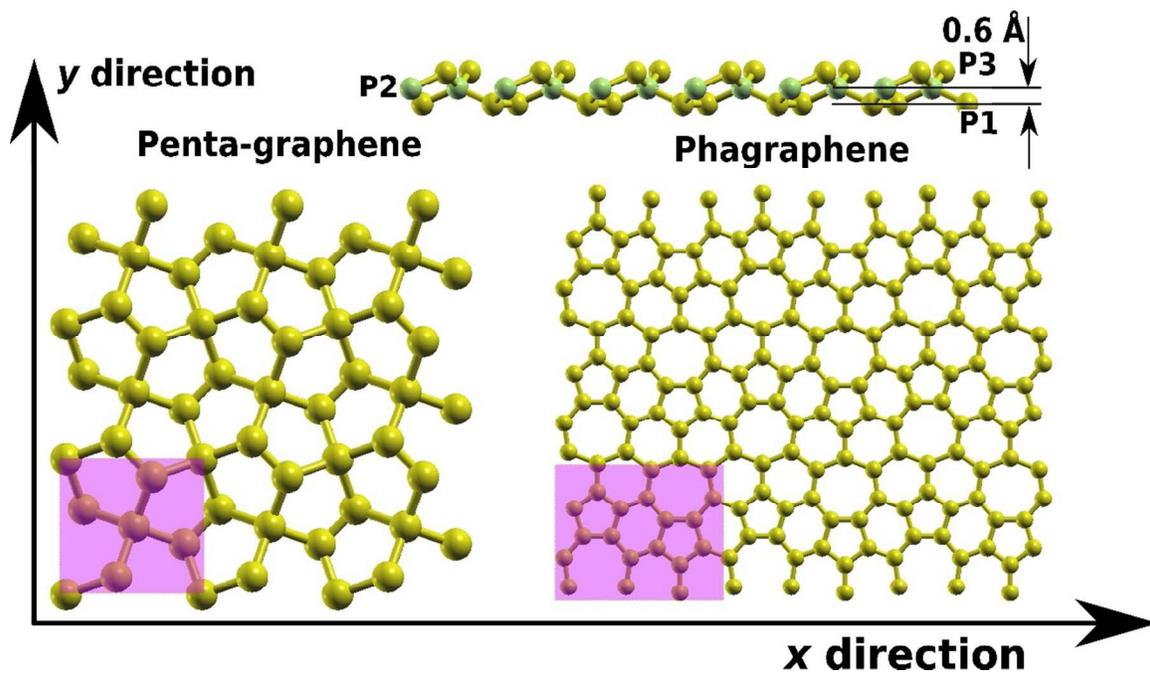| | Graphene[15] | Penta-graphene | Phagraphene |
|---|---|---|---|
| $C_{11}$ | 358.1 | 275.71 | 313.21 |
| $C_{12}$ | 60.4 | -21.43 | 79.72 |
| $C_{22}$ | 358.1 | 274.03 | 328.91 |
| $C_{111}$ | -2817 | -1568.3 | -2538.4 |
| $C_{112}$ | -337.1 | 45.0851 | -679.7 |
| $C_{222}$ | -2693.3 | -1486.1 | -2786 |
| $C_{1111}$ | 13416.2 | -3685 | 13811 |
| $C_{1112}$ | 759 | 1655.6 | 5372.8 |
| $C_{1122}$ | 2582.8 | 533.07 | 1212.5 |
| $C_{2222}$ | 10358.9 | -5633.1 | 20486 |
| $C_{11111}$ | -31383.8 | 67620 | -76024 |
| $C_{11112}$ | -88.4 | -16680 | -25997 |
| $C_{11122}$ | -12960.5 | -3496 | -27871 |
| $C_{12222}$ | -13046.6 | -27662 | -29786 |
| $C_{22222}$ | -33446.7 | 86763 | -169270 |

10

Figure 1. Schematics of the atomic structures for penta-graphene and phagraphene. Unit cells are shown in pink. Side views of penta-graphene are shown on the top of this figure with three planes of atom. The atoms in P2 plane are marked in green.
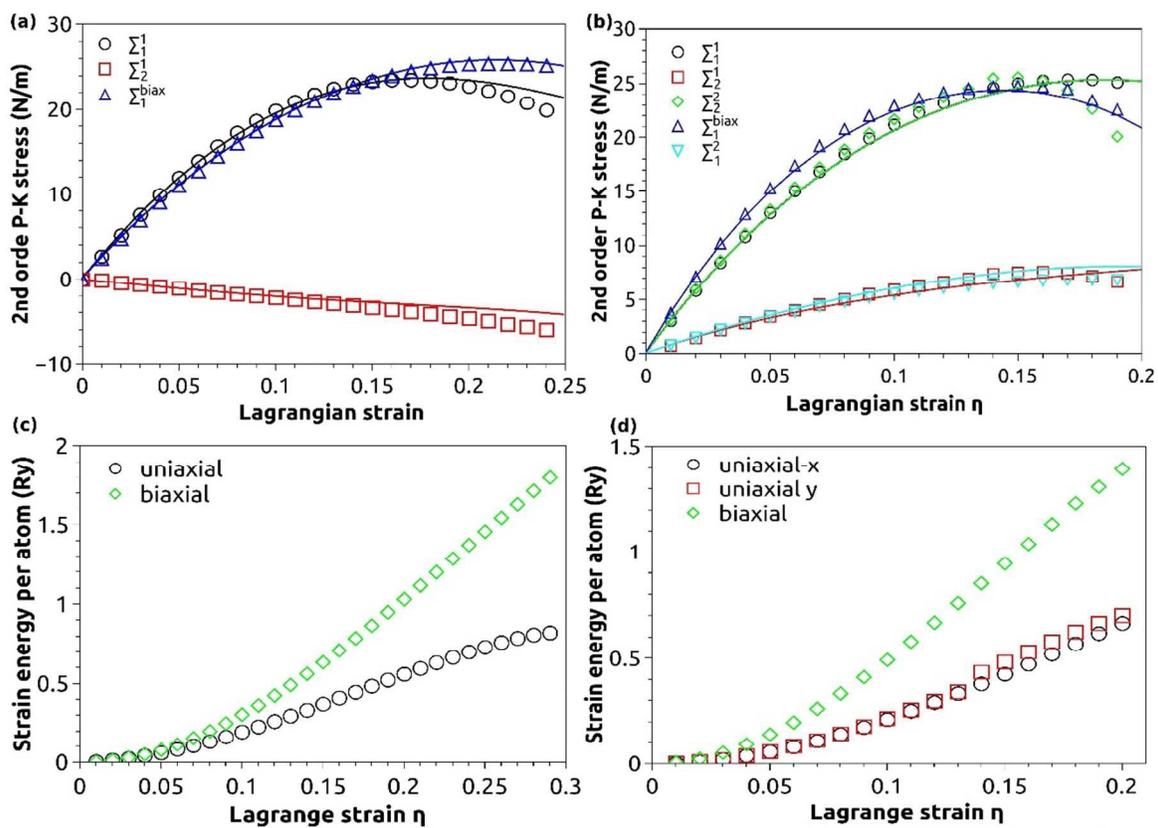
Figure 2. Stress strain curves for penta-graphene (a) and phagraphene (b). Energy–strain responses for penta-graphene (c) and phagraphene (d).
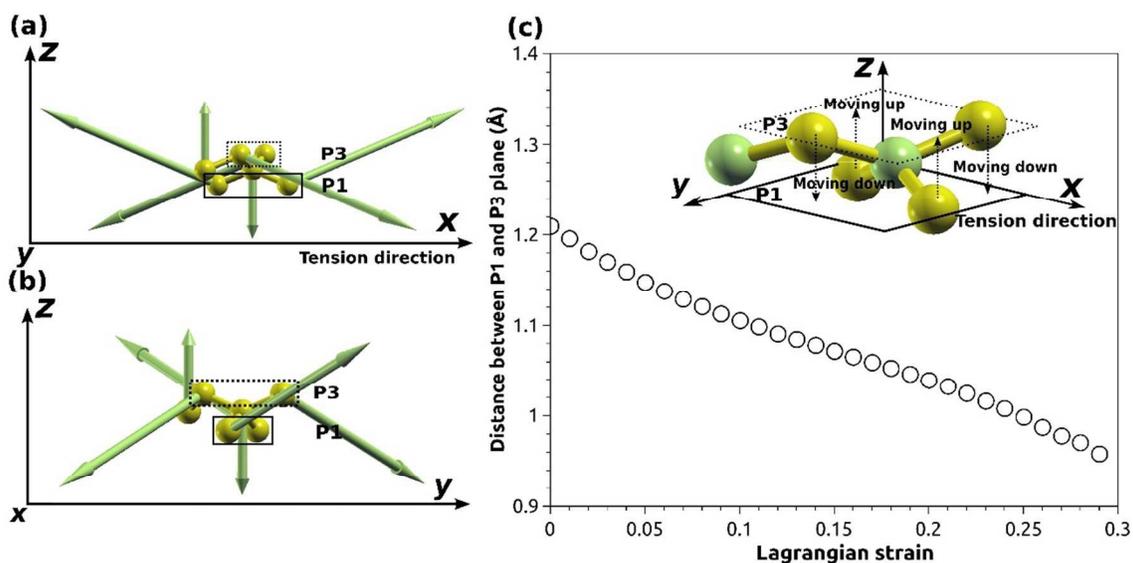
Figure 3. (a) and (b) show the atomic configurations and residual Hellman–Feynman force on each atom in penta-graphene for a uniaxial tensile strain of 7%. (c) The distance between the P1 and P3 planes in penta-graphene as a function of applied biaxial. The inset shows the unit cell of penta-graphene with atoms in P2 plane marked in green. Under the influence of biaxial strain, the atoms in the P3 plane tends to move in the -$z$ direction (move down), whereas those in the P1 plane tends to move in the +$z$ direction (move up).
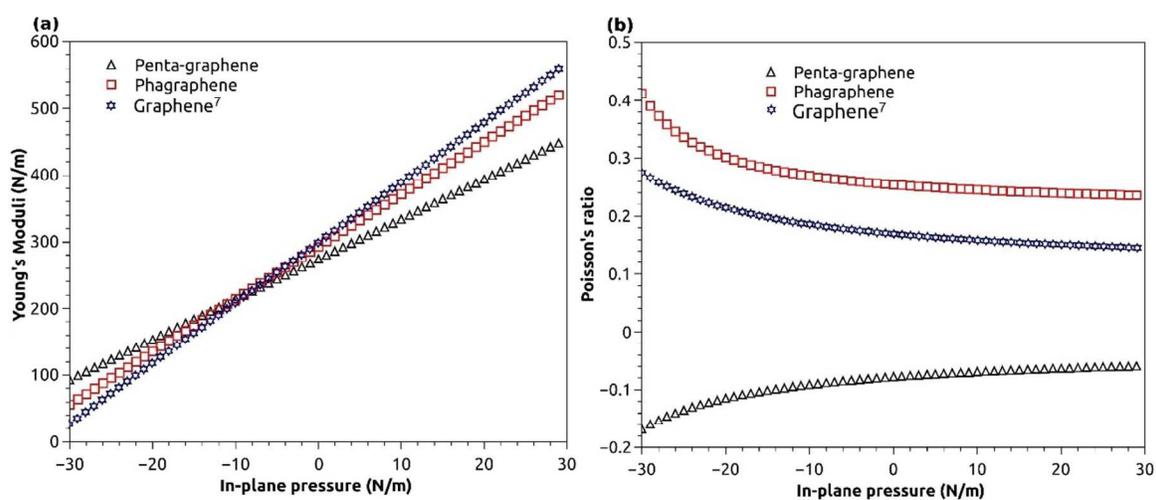
Figure 4. (a) Second-order elastic moduli (b) and Poisson's ratio as a function of the in-plane pressure for graphene, penta-graphene, and phagraphene.
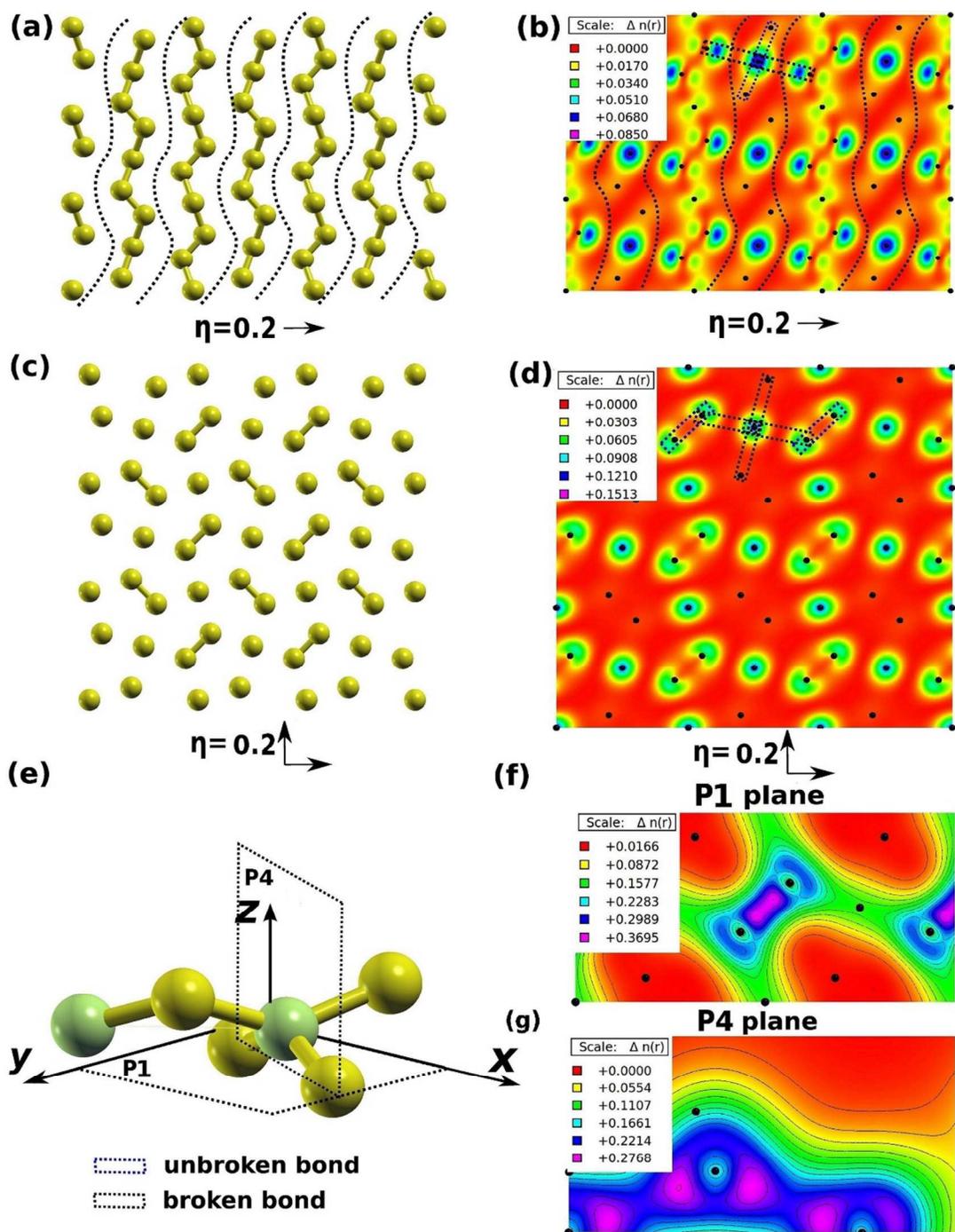
Figure 5. (a) The atomic configuration of penta-graphene after a uniaxial strain of 0.2 in the *x*-direction. The dashed lines show the fracture pathways. (b) Virtual STM image of the atomic configuration shown in subfigure (a). (c) The atomic configuration of penta-graphene after a biaxial strain of 0.2 (d) Virtual STM image of atomic configuration in subfigure (b) with a bias voltage 0.136 eV. (e) Position of P1 and P4 plane in penta-graphene shown by dotted line. (f) Charge density plot of penta-graphene in the P1 plane (f) and P4 plane (g). The "Scale" legend represents the relative density of electrons, the unit for electron density is $1/Å^2$.
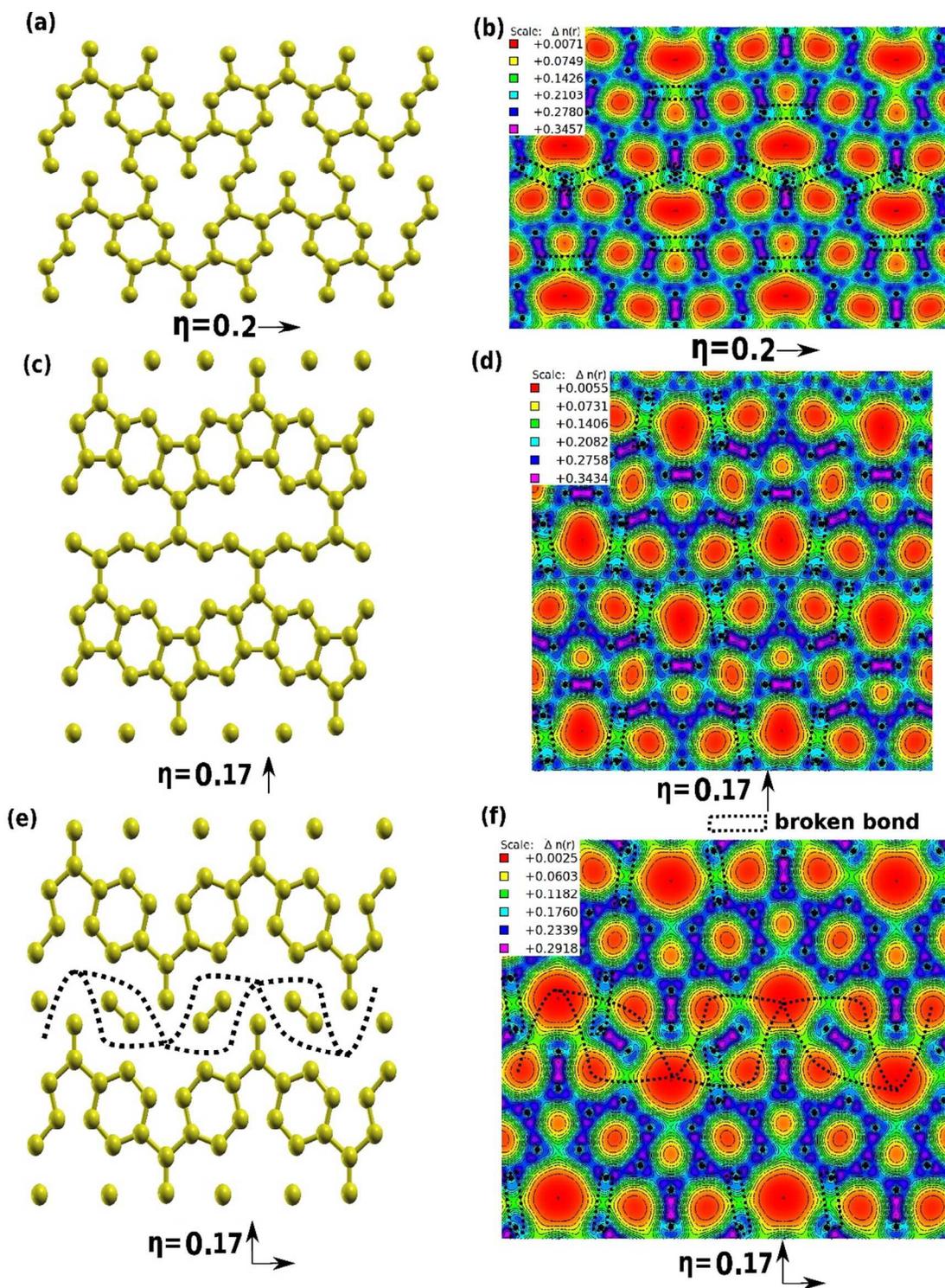
Figure 6. Charge density plot of phagraphene after (a) *x*-uniaxial tension for a strain of 0.2, (b) *y*-uniaxial tension for a strain of 0.17, and (c) biaxial tension for a strain of 0.17. The dashed lines show the fracture pathways. The broken bonds are emphasized by black rectangles. The "Scale" legend represents the relative density of electrons, the unit for electron density is $1/Å^2$.